

Quantum decoherence by magnetic fluctuations in a candidate axion insulator

Ruben Saatjian,¹ Kohtaro Yamakawa,² Ryan S. Russell,¹ James G. Analytis,² and John W. Harter^{1,*}

¹*Materials Department, University of California, Santa Barbara, California 93106, USA*

²*Department of Physics, University of California, Berkeley, California 94720, USA*

(Dated: July 8, 2024)

In magnetic topological insulators, spontaneous time-reversal symmetry breaking by intrinsic magnetic order can open an energy gap in the topological surface spectrum. In the resulting state, exotic properties like axion electrodynamics, the quantum anomalous Hall effect, and other topological magnetoelectric responses are expected to emerge. A detailed understanding of the magnetic order and its coupling to the topological surface states is essential to harness and tune these properties. Here, we leverage near-resonant electric quadrupole optical second harmonic generation to probe magnetic fluctuations in the candidate axion insulator $\text{EuSn}_2(\text{As,P})_2$ across its antiferromagnetic phase boundary. We observe a pronounced dimensional crossover in the quantum decoherence induced by magnetic fluctuations, where two-dimensional in-plane ferromagnetic correlations at high temperatures give way to three-dimensional long-range order at the Néel temperature. We also observe the breaking of rotational symmetry within the long-range-ordered antiferromagnetic state and map out the resulting spatial domain structure. More generally, we demonstrate the unique capabilities of nonlinear optical spectroscopy to study quantum coherence and fluctuations in magnetic quantum materials.

Magnetic topological insulators represent a fascinating class of quantum materials that combine a topologically nontrivial electronic structure with magnetic order [1]. Under these conditions, spontaneous time-reversal symmetry breaking by the magnetism can promote a range of novel phenomena, including axion electrodynamics [2–6], the quantum anomalous Hall effect [7–10], chiral topological superconductivity [11], and the generation of ideal Weyl nodes [12–14]. These states have unique functionalities and tunability, with potential applications in spintronic devices and other advanced technologies. The first experimental observation of such physics occurred in conventional topological insulators extrinsically doped with dilute magnetic ions [8–10], but this necessarily introduces substantial disorder into the material. More recently, intrinsic magnetic topological insulators, which are stoichiometric compounds with native long-range magnetic order, have garnered significant interest as clean and tunable material platforms that may facilitate the observation and study of topological magnetoelectric phenomena at higher temperature scales.

Although still rare, two dominant intrinsic magnetic topological insulator material families have emerged in recent years: MnBi_2Te_4 and related materials, the subject of considerable early work [6, 15–19], and a series of Eu-based Zintl materials including EuIn_2As_2 , EuCd_2As_2 , EuSn_2As_2 , and EuSn_2P_2 [5, 12–14, 20–23]. This latter family has a layered structure with Eu^{2+} ions forming a triangular lattice sandwiched between two covalently-bonded buckled honeycomb layers, such as $(\text{SnAs})_2^{2-}$, from which the topological bands are derived. Magnetism arises from half-filled $4f^7$ subshells on the Eu^{2+} ions. These localized high-spin ($S = 7/2$) moments align ferromagnetically in the plane and antiferromagnetically out of the plane [Fig. 1(a)], resulting in long-range A-type

antiferromagnetism below a Néel temperature T_N that ranges from 10 K to 30 K, depending on material. The distinct spatial separation of magnetic and topological electronic states in these materials raises the possibility of precise magnetic control over the electronic topology, for example through the direction of magnetization [5].

In this work, we study fluctuations and symmetry breaking by the magnetic degrees of freedom in the Eu-based materials using near-resonant electric quadrupole optical second harmonic generation (SHG). We focus on the $\text{EuSn}_2(\text{As,P})_2$ compounds, which have the highest reported T_N (24 K and 30 K for the Sn and P endmembers, respectively [20, 21]). We measure the quantum decoherence induced by magnetic fluctuations across T_N and find a dimensional crossover from short-range two-dimensional in-plane ferromagnetic correlations above T_N to three-dimensional long-range antiferromagnetic order below it. Within the low-temperature antiferromagnetic phase, we detect broken rotational symmetry due to global alignment of the in-plane magnetic moments, and map out the corresponding spatial domain patterns. Our results motivate several routes to tune the magnetism in this series of materials, paving the way for the potential control of topological magnetoelectric properties. More broadly, we showcase the capabilities of nonlinear optical spectroscopy to access the degree of quantum coherence of magnetic fluctuations in quantum materials.

Single crystals of EuSn_2As_2 , EuSn_2P_2 , and the 1:1 alloy EuSn_2AsP were prepared by a flux method similar to Ref. 24. All three materials show nearly-identical nonlinear optical responses, and magnetic susceptibility measurements show clear signatures of antiferromagnetic transitions with T_N closely matching previously reported values [20–22, 24]. Further details of sample synthesis and characterization can be found in the Supplemental

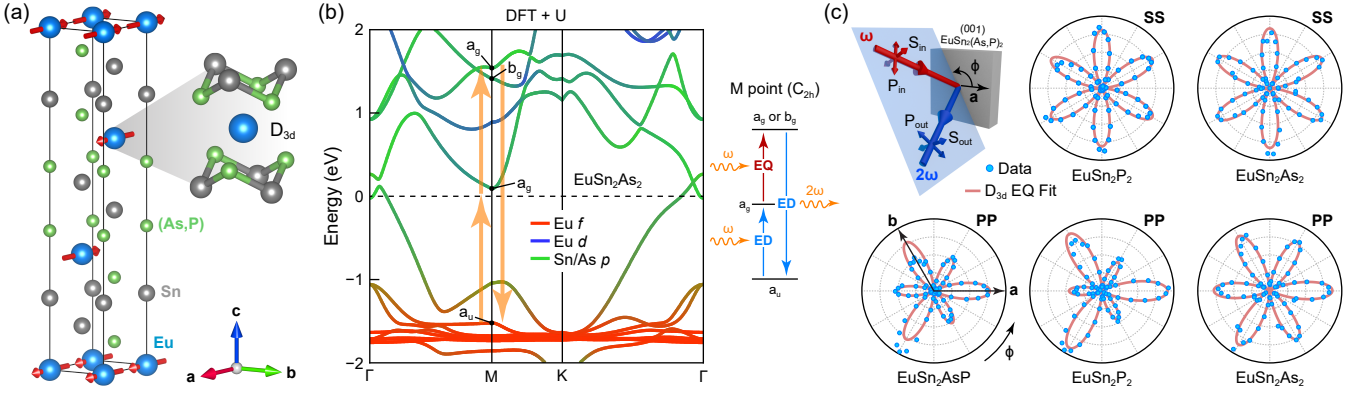


FIG. 1. Crystal and electronic structure of $\text{EuSn}_2(\text{As,P})_2$ and RA-SHG patterns. (a) Crystal structure showing half of the conventional magnetic unit cell. Red arrows depict Eu^{2+} local magnetic moments, which lie within the plane along the a axis. Moments are aligned within each plane and antialigned with neighboring planes, forming long-range A-type antiferromagnetism. The inset illustrates the local environment surrounding the Eu^{2+} ions, showing D_{3d} site symmetry. (b) Orbital-resolved electronic band structure of EuSn_2As_2 from DFT. The calculation was performed for the primitive unit cell (ferromagnetic moment alignment), but k -points are referenced to the conventional unit cell. Vertical arrows highlight optical transitions near the M point contributing to near-resonant SHG. The irreducible representations of the states participating in the resonances are labeled. The right inset shows a simplified energy level diagram of SHG involving both electric dipole (ED) and electric quadrupole (EQ) optical transitions. (c) Parallel polarization RA-SHG patterns for all three materials at 50 K. The top left panel defines the oblique incidence scattering geometry. The top row shows $S_{\text{in}}\text{-}S_{\text{out}}$ (SS) polarization patterns and the bottom row shows $P_{\text{in}}\text{-}P_{\text{out}}$ (PP) polarization patterns.

Materials. Density functional theory (DFT) calculations were performed with the Vienna Ab initio Simulation Package (VASP) using the supplied projector augmented wave potentials within the generalized gradient approximation, the experimental structural parameters [20], a 400 eV energy cutoff, and a $6 \times 6 \times 6$ k -point mesh. To match the experimental energy position of the Eu 4*f* bands, a Hubbard parameter $U = 5.0$ eV was employed [22]. Measuring the rotational anisotropy of optical SHG (RA-SHG) is a precise method to access the nonlinear optical susceptibility tensor and deduce the point group symmetries of a material. Using RA-SHG, tensor elements can be tracked across a wide temperature range to reveal minute changes in order, symmetry, dimensionality, and the strength of interactions in a sample [25–28]. With this goal, RA-SHG experiments were performed on freshly-cleaved samples in an optical cryostat using an ultrafast laser supplying 40-fs pulses at a 50-kHz repetition rate with a center wavelength of 800 nm and a fluence of ~ 1 mJ/cm². The extreme sensitivity of SHG can be further enhanced near resonances, strengthening the SHG response by orders of magnitude and amplifying signatures of states involved in the resonant transition. As Fig. 1(b) demonstrates, 800 nm excitation (1.55 eV) is nearly resonant with several energy transitions involving Eu 4*f* and 5*d* orbitals at the M point in the first Brillouin zone, gaining us direct access to the magnetic degrees of freedom.

Figure 1(c) illustrates the RA-SHG experimental scattering geometry and corresponding data for all three samples. In the $S_{\text{in}}\text{-}S_{\text{out}}$ channel, six equal lobes appear,

while in the $P_{\text{in}}\text{-}P_{\text{out}}$ channel, the underlying 3-fold rotational symmetry of the crystallographic point group D_{3d} ($\bar{3}m$) is revealed through alternating large and small lobes. Oblique incidence is key to the appearance of this alternation; normal incidence measurements would fail to capture this lower symmetry and instead yield six equal lobes as in the $S_{\text{in}}\text{-}S_{\text{out}}$ data. The measured SHG intensity is relatively strong, which is unusual because D_{3d} is centrosymmetric and leading-order bulk electric dipole SHG—the usual source of strong nonlinear optical responses—is hence excluded by symmetry. Among the most likely higher-order nonlinear responses are surface electric dipole, bulk magnetic dipole, and bulk electric quadrupole SHG (EQ-SHG) [26]. Surface SHG typically arises from slight atomic distortions at the surface of a material and is therefore generally weakly dependent on temperature. We exclude this possibility based on the striking temperature dependence that we observe and discuss below. We also exclude magnetic dipole SHG due to the presence of time-reversal symmetry (in combination with a lattice translation below T_N). This leaves EQ-SHG as the primary nonlinear response channel in $\text{EuSn}_2(\text{As,P})_2$. Recently, EQ-SHG has proven to be a powerful tool for probing the intricate magnetic properties of topological materials such as magnetic Weyl semimetals [28].

EQ-SHG is described by a fourth-rank nonlinear optical susceptibility tensor χ_{ijkl}^{EQ} that relates the induced nonlinear polarization density in a material $P_i(2\omega)$ to two powers of the incident electric field $E_j(\omega)$ via the equation $P_i(2\omega) = \chi_{ijkl}^{\text{EQ}} E_j(\omega) \nabla_k E_l(\omega)$ [26]. Within point

group D_{3d} and with additional permutation symmetries adapted from Ref. 29, we may calculate the explicit angular dependence of the RA-SHG patterns. For the two parallel polarization channels shown in Fig. 1(c), we obtain $I_{SS}(\phi) = |\alpha \sin(3\phi)|^2$ and $I_{PP}(\phi) = |\alpha \cos(3\phi) + \beta|^2$, where $\alpha = \chi_{xxxx}^{\text{EQ}} \cos(\theta)$, $\beta = (\chi_{xxxx}^{\text{EQ}} - \chi_{xxzz}^{\text{EQ}}) \sin(\theta)$, ϕ is the azimuthal angle of the scattering plane, and θ is the angle of incidence relative to the sample surface normal. Fits of the data to these functional forms show excellent agreement, as demonstrated in Fig. 1(c). Further details of the tensor symmetry analysis can be found in the Supplemental Materials.

A defining characteristic of EQ-SHG is the inclusion of an optical transition between two states of the same parity, a good quantum number in centrosymmetric systems. Such excitations are forbidden in conventional electric dipole transitions. With this symmetry condition in mind, we examine the irreducible representations of wave functions calculated by DFT for EuSn_2As_2 and identify the M point as the likely source of near-resonant EQ-SHG at 800 nm. At this high-symmetry point, with little group C_{2h} ($2/m$), an electron occupying a Eu f_{xyz} , f_{xz^2} , or $f_{x(x^2-3y^2)}$ orbital (odd-parity a_u symmetry) can be excited to an unoccupied even-parity a_g virtual state through resonant electric dipole absorption at ~ 1.5 eV, further excited by a parity-preserving electric quadrupole transition to a higher a_g or b_g virtual state (both are allowed), and then return to its initial state through resonant electric dipole emission at ~ 3 eV. The overall EQ-SHG process is illustrated in Fig. 1(b). The participating unoccupied virtual states have partial ($\sim 20\%$) Eu $5d$ character but majority Sn and As p character. Thus, in real space we may interpret the initial optical transition as a charge-transfer excitation in which an electron is removed from a tightly-bound Eu $4f$ orbital and added to the extended $(\text{SnAs})_2$ network. This leaves behind a Eu atom in a $4f^6$ configuration with a reduced spin. The reduced moment on the spin lattice represents a localized magnetic excitation that will propagate outward as it becomes entangled with neighboring spin. This process of magnetic decoherence of the virtual states is expected to be sensitive to the strength and nature of the magnetic order in the system, as we detail below.

Now that near-resonant EQ-SHG has been established as the source of the strong nonlinear optical response, we turn to its temperature dependence. Figure 2 shows the total SHG intensity integrated over ϕ as a function of temperature. Several remarkable features are apparent. First, we observe a significant growth in SHG as the sample is cooled, more than doubling between room temperature and 100 K. Second, below ~ 100 K a broad high-intensity hump exists with large associated fluctuations. Third, upon traversing the magnetic transition temperature T_N , an extremely sharp SHG peak occurs. Finally, as temperature is further lowered in the magnetically-ordered phase, the SHG intensity decreases again. Such

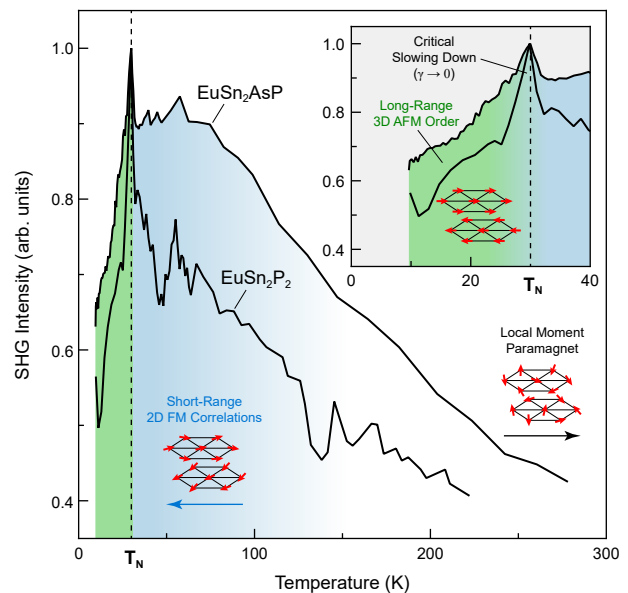


FIG. 2. Temperature dependence of SHG. Upon cooling from room temperature, the SHG intensity increases dramatically. Below ~ 100 K, a broad hump (most apparent in EuSn_2AsP) and large fluctuations (most apparent in EuSn_2P_2) are observed. We identify these features with the emergence of fluctuating short-range ferromagnetic correlations within the Eu planes (blue). Within ~ 2 K of T_N , a pronounced peak appears, which we attribute to critical slowing down at the magnetic phase transition, as discussed in the main text. Below T_N , the SHG intensity decreases as long-range three-dimensional antiferromagnetic order freezes in (green). The inset shows a close-up view of the low-temperature region.

behavior resembles a linear magnetic susceptibility measurement, but we emphasize that here we are measuring a nonlinear optical susceptibility that is not directly sensitive to the magnetic degrees of freedom. Generally, one may expect a slight change in the SHG intensity below the magnetic ordering temperature, but that is not what we observe. Instead, we appear to be sensitive to *fluctuations* of the magnetic order. In particular, we observe an increase in SHG associated with the growth of short-range two-dimensional ferromagnetic correlations within the individual Eu layers above T_N . Large fluctuations are expected in this regime because true long-range order is forbidden by the Mermin-Wagner theorem [30]. Strong in-plane ferromagnetic fluctuations below ~ 100 K have also been detected in the related material EuCd_2As_2 by muon spin relaxation, and it has been suggested that these short-range magnetic fluctuations are sufficient to induce topological properties even in the absence of long-range magnetic order [12, 31]. At T_N , we observe a dimensional crossover as the short-range in-plane ferromagnetic correlations give rise to true long-range three-dimensional antiferromagnetic order. At the transition, critical fluctuations are expected to be largest, and this is reflected in the observed sharp SHG peak. Finally, upon

further cooling, the long-range magnetic order grows in strength and fluctuations accordingly diminish, as does the SHG intensity. Thus, taken as a whole, our observations are consistent with a pronounced sensitivity of EQ-SHG to fluctuations of the magnetic degrees of free-

dom, rather than the magnetic order itself.

To interpret this result, we examine the expression for the EQ-SHG nonlinear optical susceptibility tensor derived from perturbation theory [32]:

$$\chi_{ijkl}^{\text{EQ}}(2\omega, \omega, \omega) = \frac{N}{2\epsilon_0 \hbar^2} \sum_{m\nu n} \left(\rho_{mm}^{(\text{eq})} - \rho_{\nu\nu}^{(\text{eq})} \right) \frac{\langle m | \mu_i | n \rangle \langle n | Q_{kl} | \nu \rangle \langle \nu | \mu_j | m \rangle}{[(\omega_{nm} - 2\omega) - i\gamma_{nm}] [(\omega_{\nu m} - \omega) - i\gamma_{\nu m}]},$$

where N is the electron density, m , ν , and n label eigenstates, $\rho_{nm}^{(\text{eq})}$ is the equilibrium density matrix, μ_i and Q_{ij} are components of the electric dipole and quadrupole operators, respectively, $\omega_{nm} = (E_n - E_m)/\hbar$, and γ_{nm} is a phenomenological parameter introduced to account for environmental degrees of freedom that contribute to quantum decoherence but are not explicitly included in the density matrix. More precisely, the density matrix obeys the quantum master equation

$$\dot{\rho}_{nm} = \frac{1}{i\hbar} [\mathcal{H}, \rho]_{nm} - \gamma_{nm} \left(\rho_{nm} - \rho_{nm}^{(\text{eq})} \right),$$

showing that γ_{nm} parameterizes quantum coherence through the rate at which off-diagonal density matrix elements decay in time: $\rho_{nm}(t) \propto e^{-i\omega_{nm}t} e^{-\gamma_{nm}t}$. Here, the density matrix captures orbital (charge) eigenstates but not magnetism, so quantum decoherence primarily arises from interactions with the background magnetic environment. As shown above, the SHG signal is dominated by a near resonance at the M point, where both $\omega_{nm} \approx 2\omega$ and $\omega_{\nu m} \approx \omega$. This significantly amplifies the effects of the γ parameters appearing in the denominator of the susceptibility expression. In fact, these are the only parameters that can appreciably influence the temperature dependence of SHG, as $\rho_{mm}^{(\text{eq})} - \rho_{\nu\nu}^{(\text{eq})} = 1$ because m is occupied and ν is unoccupied, and the electric dipole and quadrupole matrix elements in the numerator are not expected to change significantly with temperature. Thus, we see that near-resonant EQ-SHG is acutely sensitive to the quantum decoherence induced by magnetic fluctuations in the system, as we have inferred from our temperature dependence measurements.

A hallmark of second-order phase transitions is the phenomenon of ‘‘critical slowing down,’’ a significant increase in the time it takes for a system to respond to perturbations or to return to equilibrium. In the critical regime, the free energy is flat and the dynamics of the system become extremely slow. Within the context of a magnetic transition, this occurs when locally-fluctuating moments become entangled with their neighbors at increasingly large distances. Both the correlation length $\xi \propto |T - T_c|^{-\nu}$ and the correlation time $\tau \propto \xi^z$ diverge, with critical exponents ν and z , respectively [33]. In an

ideal system, this results in $\gamma \rightarrow 0$ at the critical temperature, which we propose as the likely origin for the sharp peak in SHG that we observe at T_N . We emphasize that within this interpretation, the growth of SHG as temperature approaches T_N is the result of an increase in the *lifetime* of magnetic fluctuations, not an increase in their amplitude. We can place a rough upper bound on the coherence time τ of the $4f^7 \rightarrow 4f^6$ magnetic excitation caused by the charge-transfer optical transition. We observe an $O(1)$ change in SHG over the measured temperature range, which implies that γ must be at least of the same order as $\Delta\omega$, the spectral width of the ultrafast laser. Thus, we calculate $\tau \sim 1/\gamma < 1/\Delta\omega \sim 16$ fs. This value is comparable to the excitation lifetime of an isolated magnetic atom bound to a metallic substrate, as measured by inelastic tunneling spectroscopy, where it was suggested that the short lifetime was due to hybridization with metallic bands, leading to efficient electron-electron interactions that relax the magnetic state of the atom [34]. $\text{EuSn}_2(\text{As,P})_2$ is also metallic, and indeed it has been suggested that the magnetic exchange coupling in the material is mediated by conduction electrons via the Ruderman–Kittel–Kasuya–Yosida (RKKY) interaction [20, 35]. Thus, we may also expect a similarly short magnetic excitation lifetime due to coupling to conduction electrons.

According to the celebrated fluctuation-dissipation theorem, there is a close relationship between the imaginary part of a linear susceptibility and the power spectral density of fluctuations of that susceptibility’s conjugate observable [33]. No such theorem exists for nonlinear susceptibilities, where the imaginary part does not represent dissipation because the time-average of $\mathbf{E}(\omega) \cdot \mathbf{J}(2\omega)$ is necessarily zero [36]. It has been theoretically shown, however, that nonlinear responses are much more sensitive than linear responses to semiclassical chaotic behavior through the interference of multiple dynamical Liouville-space trajectories [37]. The second-order susceptibility, for example, is directly related to the stability matrix of a system and its associated Lyapunov exponents quantifying the system’s sensitivity to initial conditions. Our measurements largely affirm this notion,

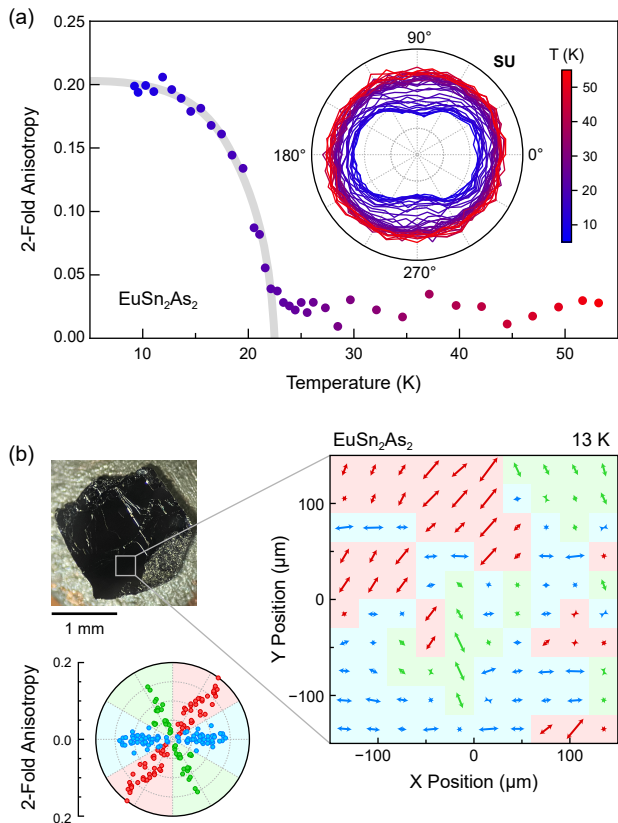


FIG. 3. Spontaneous rotational symmetry breaking in EuSn_2As_2 . (a) Temperature dependence of the 2-fold rotational anisotropy that emerges at the antiferromagnetic phase transition. The inset shows $S_{\text{in}}-U_{\text{out}}$ (SU) RA-SHG patterns for each temperature, and the main panel shows the corresponding 2-fold anisotropy versus temperature. The gray curve is a guide to the eye, showing an order-parameter-like onset below T_N . (b) Spatial map of rotational symmetry breaking. RA-SHG patterns were acquired on a 10×10 grid spanning a $300 \times 300 \mu\text{m}$ area. At each grid point, the amplitude and direction of the 2-fold anisotropy was extracted (represented by the length and direction, respectively, of the double-headed arrows). The upper left inset shows a photograph of the sample with the mapped region identified, and the lower left inset shows a polar plot of the anisotropy sorted by direction into three symmetry-equivalent antiferromagnetic domains (red, green, and blue). The map reveals static domains with sizes on the order of $\sim 100 \mu\text{m}$.

demonstrating that, at least near resonances, the nonlinear optical response of a material can be significantly influenced by the dynamics of fluctuations of some order parameter of the material, even when that order is not the conjugate observable of the susceptibility. We expect that this principle is generally applicable, and that under sufficiently resonant conditions, the nonlinear optical response of a material can be harnessed to study fluctuations, dynamics, and quantum coherence across many types of second-order phase transitions.

Within the long-range ordered antiferromagnetic phase

below T_N , the Eu^{2+} moments of $\text{EuSn}_2(\text{As,P})_2$ become in-plane aligned. This necessarily results in spontaneous breaking of the $\bar{3}$ symmetry axis of the crystal, as the moments must choose one of three equivalent crystallographic directions along which to orient themselves. Rotational symmetry breaking can generally be revealed through RA-SHG patterns, which are exceptionally sensitive to point group symmetries [26]. As Fig. 3(a) demonstrates, we indeed observe the onset of rotational symmetry breaking below T_N in RA-SHG patterns, with a clear order-parameter-like temperature dependence. Here we measure the unpolarized SHG output (U_{out}) because, in this case, a fully isotropic (i.e. circular) response is expected in the high-symmetry phase, degenerating into a 2-fold “peanut-like” shape when the rotational symmetry axis is lost. Further details on the quantification of the 2-fold anisotropy can be found in the Supplemental Materials. We attribute this observation to two possible mechanisms, both involving spin-orbit coupling. In the first mechanism, strong coupling of the globally-aligned spins to the initial-state f orbitals (f_{xyz} , f_{xz^2} , and $f_x(x^2-3y^2)$) shifts their energies, and this manifests as slight changes to the optical resonance condition for different polarization angles. In the second mechanism, the global alignment of moments influences the quantum coherence of different initial-state f orbitals. Given that the 2-fold anisotropy we observe is almost of the same magnitude as the SHG intensity itself ($\sim 20\%$), we believe the second scenario is more likely. Accompanying spontaneous symmetry breaking is the formation of magnetic domains transforming into each other by the broken symmetry element. Optical imaging of antiferromagnetic domains is typically very challenging because of the absence of a net magnetization, with SHG being one of the few known techniques for doing so [38, 39]. Figure 3(b) shows a spatial RA-SHG mapping over a $300 \times 300 \mu\text{m}$ area that reveals these domains. We find a roughly equal distribution of all three possible domain orientations, with an approximate domain length scale of $\sim 100 \mu\text{m}$. Thermal cycling across T_N generates completely new domain patterns, as shown in the Supplemental Materials, suggesting domain boundaries are not pinned by disorder.

In conclusion, we have harnessed near-resonant EQ-SHG to probe the intricate magnetic dynamics in the candidate axion insulator $\text{EuSn}_2(\text{As,P})_2$. By examining the material across its antiferromagnetic phase boundary, we have revealed a pronounced dimensional crossover in the quantum decoherence induced by magnetic fluctuations, with two-dimensional in-plane ferromagnetic correlations at high temperatures transitioning to three-dimensional long-range order below T_N . Moreover, we have observed an unusually sharp SHG peak right at the magnetic phase boundary that we attribute to the phenomenon of critical slowing down, where the dynamics of the system become extremely slow and the correlation length and time diverge. The quantum coherence time

of the charge-transfer $4f^7 \rightarrow 4f^6$ magnetic excitation is estimated to be no more than ~ 16 fs. We conjecture that such a short lifetime is due to efficient coupling between the localized magnetic moments and the conduction electrons in $\text{EuSn}_2(\text{As,P})_2$, supporting a scenario whereby RKKY interactions mediate the magnetic exchange [20, 35]. This conclusion has important implications for the coupling strength between the magnetic order and the topological electronic states, where prior work has reported only a very weak hybridization [22]. Exotic topological boundary modes have been predicted at magnetic domain boundaries in this class of materials [5]. By leveraging the extreme sensitivity of RA-SHG, we have uncovered the clear breaking of rotational symmetry within the antiferromagnetic phase and used it to map out the spatial domain structure that emerges. Our findings help to clarify the nature of the magnetic order in this class of materials and its interactions with topological surface states, which play a critical role in realizing topological magnetoelectric phenomena. More generally, our work showcases the unique capabilities of nonlinear optical spectroscopy as a powerful tool for investigating quantum coherence and fluctuations in magnetic quantum materials.

ACKNOWLEDGMENTS

This work was supported by the U.S. Air Force Office of Scientific Research (AFOSR) under Award No. FA9550-22-1-0270. The research reported here made use of the shared facilities of the Materials Research Science and Engineering Center (MRSEC) at UC Santa Barbara: NSF DMR-2308708. The UC Santa Barbara MRSEC is a member of the Materials Research Facilities Network (www.mrfn.org).

* Corresponding author: harter@ucsb.edu

- [1] Y. Tokura, K. Yasuda, A. Tsukazaki. Magnetic topological insulators. *Nat. Rev. Phys.* **1**, 126 (2019).
- [2] A. M. Essin, J. E. Moore, D. Vanderbilt. Magnetoelectric Polarizability and Axion Electrodynamics in Crystalline Insulators. *Phys. Rev. Lett.* **102**, 146805 (2009).
- [3] R. Li, J. Wang, X.-L. Qi, S.-C. Zhang. Dynamical axion field in topological magnetic insulators. *Nat. Phys.* **6**, 284 (2010).
- [4] M. Mogi, M. Kawamura, R. Yoshimi, A. Tsukazaki, Y. Kozuka, N. Shirakawa, K. S. Takahashi, M. Kawasaki, Y. Tokura. A magnetic heterostructure of topological insulators as a candidate for an axion insulator. *Nat. Mater.* **16**, 516 (2017).
- [5] Y. Xu, Z. Song, Z. Wang, H. Weng, X. Dai. Higher-Order Topology of the Axion Insulator EuIn_2As_2 . *Phys. Rev. Lett.* **122**, 256402 (2019).
- [6] D. Zhang, M. Shi, T. Zhu, D. Xing, H. Zhang, J. Wang. Topological Axion States in the Magnetic Insulator MnBi_2Te_4 with the Quantized Magnetoelectric Effect. *Phys. Rev. Lett.* **122**, 206401 (2019).
- [7] R. S. K. Mong, A. M. Essin, J. E. Moore. Antiferromagnetic topological insulators. *Phys. Rev. B* **81**, 245209 (2010).
- [8] C.-X. Liu, X.-L. Qi, X. Dai, Z. Fang, S.-C. Zhang. Quantum Anomalous Hall Effect in $\text{Hg}_{1-y}\text{Mn}_y\text{Te}$ Quantum Wells. *Phys. Rev. Lett.* **101**, 146802 (2008).
- [9] R. Yu, W. Zhang, H.-J. Zhang, S.-C. Zhang, X. Dai, Z. Fang. Quantized Anomalous Hall Effect in Magnetic Topological Insulators. *Science* **329**, 61 (2010).
- [10] C.-Z. Chang, J. Zhang, X. Feng, J. Shen, Z. Zhang, M. Guo, K. Li, Y. Ou, P. Wei, L.-L. Wang, Z.-Q. Ji, Y. Feng, S. Ji, X. Chen, J. Jia, X. Dai, Z. Fang, S.-C. Zhang, K. He, Y. Wang, L. Lu, X.-C. Ma, Q.-K. Xue. Experimental Observation of the Quantum Anomalous Hall Effect in a Magnetic Topological Insulator. *Science* **340**, 167 (2013).
- [11] X.-L. Qi, T. L. Hughes, S.-C. Zhang. Chiral topological superconductor from the quantum Hall state. *Phys. Rev. B* **82**, 184516 (2010).
- [12] J.-Z. Ma, S. M. Nie, C. J. Yi, J. Jandke, T. Shang, M. Y. Yao, M. Naamneh, L. Q. Yan, Y. Sun, A. Chikina, V. N. Strocov, M. Medarde, M. Song, Y.-M. Xiong, G. Xu, W. Wulfhekel, J. Mesot, M. Reticcioli, C. Franchini, C. Mudry, M. Muller, Y. G. Shi, T. Qian, H. Ding, M. Shi. Spin fluctuation induced Weyl semimetal state in the paramagnetic phase of EuCd_2As_2 . *Sci. Adv.* **5**, eaaw4718 (2019).
- [13] J.-R. Soh, F. de Juan, M. G. Vergniory, N. B. M. Schroter, M. C. Rahn, D. Y. Yan, J. Jiang, M. Bristow, P. Reiss, J. N. Blandy, Y. F. Guo, Y. G. Shi, T. K. Kim, A. McCollam, S. H. Simon, Y. Chen, A. I. Coldea, A. T. Boothroyd. Ideal Weyl semimetal induced by magnetic exchange. *Phys. Rev. B* **100**, 201102(R) (2019).
- [14] N. H. Jo, B. Kuthanazhi, Y. Wu, E. Timmons, T.-H. Kim, L. Zhou, L.-L. Wang, B. G. Ueland, A. Palasyuk, D. H. Ryan, R. J. McQueeney, K. Lee, B. Schruck, A. A. Burkov, R. Prozorov, S. L. Bud'ko, A. Kaminski, P. C. Canfield. Manipulating magnetism in the topological semimetal EuCd_2As_2 . *Phys. Rev. B* **101**, 140402(R) (2020).
- [15] Y. J. Chen, L. X. Xu, J. H. Li, Y. W. Li, H. Y. Wang, C. F. Zhang, H. Li, Y. Wu, A. J. Jiang, C. Chen, S. W. Jung, C. Cacho, Y. H. Mao, S. Liu, M. X. Wang, Y. F. Guo, Y. Xu, Z. K. Liu, L. X. Yang, Y. L. Chen. Topological Electronic Structure and Its Temperature Evolution in Antiferromagnetic Topological Insulator MnBi_2Te_4 . *Phys. Rev. X* **9**, 041040 (2019).
- [16] J. Li, Y. Li, S. Du, Z. Wang, B.-L. Gu, S.-C. Zhang, K. He, W. Duan, Y. Xu. Intrinsic magnetic topological insulators in van der Waals layered MnBi_2Te_4 -family materials. *Sci. Adv.* **5**, eaaw5685 (2019).
- [17] K. He. MnBi_2Te_4 -family intrinsic magnetic topological materials. *npj Quant. Mater.* **5**, 90 (2020).
- [18] Z. Jiang, J. Liu, Z. Liu, D. Shen. A review of angle-resolved photoemission spectroscopy study on topological magnetic material family of MnBi_2Te_4 . *Electron. Struct.* **4**, 043002 (2022).
- [19] S. Li, T. Liu, C. Liu, Y. Wang, H.-Z. Lu, X. C. Xie. Progress on the antiferromagnetic topological insulator MnBi_2Te_4 . *Natl. Sci. Rev.* **11**, nwac296 (2024).

- [20] M. Q. Arguilla, N. D. Cultrara, Z. J. Baum, S. Jiang, R. D. Ross, J. E. Goldberger. EuSn_2As_2 : an exfoliatable magnetic layered Zintl–Klemm phase. *Inorg. Chem. Front.* **4**, 378 (2017).
- [21] X. Gui, I. Pletikoscic, H. Cao, H.-J. Tien, X. Xu, R. Zhong, G. Wang, T.-R. Chang, S. Jia, T. Valla, W. Xie, R. J. Cava. A New Magnetic Topological Quantum Material Candidate by Design. *ACS Cent. Sci.* **5**, 900 (2019).
- [22] H. Li, S.-Y. Gao, S.-F. Duan, Y.-F. Xu, K.-J. Zhu, S.-J. Tian, J.-C. Gao, W.-H. Fan, Z.-C. Rao, J.-R. Huang, J.-J. Li, D.-Y. Yan, Z.-T. Liu, W.-L. Liu, Y.-B. Huang, Y.-L. Li, Y. Liu, G.-B. Zhang, P. Zhang, T. Kondo, S. Shin, H.-C. Lei, Y.-G. Shi, W.-T. Zhang, H.-M. Weng, T. Qian, H. Ding. Dirac Surface States in Intrinsic Magnetic Topological Insulators EuSn_2As_2 and $\text{MnBi}_{2n}\text{Te}_{3n+1}$. *Phys. Rev. X* **9**, 041039 (2019).
- [23] G. M. Pierantozzi, A. De Vita, C. Bigi, X. Gui, H.-J. Tien, D. Mondal, F. Mazzola, J. Fujii, I. Vobornik, G. Vinai, A. Sala, C. Africh, T.-L. Lee, G. Rossi, T.-R. Chang, W. Xie, R. J. Cava, G. Panaccione. Evidence of magnetism-induced topological protection in the axion insulator candidate EuSn_2P_2 . *Proc. Natl. Acad. Sci. U.S.A.* **119**, e2116575119 (2022).
- [24] S. Pakhira, M. A. Tanatar, T. Heitmann, D. Vaknin, D. C. Johnston. *A*-type antiferromagnetic order and magnetic phase diagram of the trigonal Eu spin-7/2 triangular-lattice compound EuSn_2As_2 . *Phys. Rev. B* **104**, 174427 (2021).
- [25] J. W. Harter, Z. Y. Zhao, J.-Q. Yan, D. G. Mandrus, D. Hsieh. A parity-breaking electronic nematic phase transition in the spin-orbit coupled metal $\text{Cd}_2\text{Re}_2\text{O}_7$. *Science* **356**, 295 (2017).
- [26] J. Orenstein, J. E. Moore, T. Morimoto, D. H. Torchinsky, J. W. Harter, D. Hsieh. Topology and Symmetry of Quantum Materials via Nonlinear Optical Responses. *Annu. Rev. Condens. Matter Phys.* **12**, 247 (2021).
- [27] A. Ron, E. Zoghlin, L. Balents, S. D. Wilson, D. Hsieh. Dimensional crossover in a layered ferromagnet detected by spin correlation driven distortions. *Nat. Commun.* **10**, 1654 (2019).
- [28] Y. Ahn, X. Guo, R. Xue, K. Qu, K. Sun, D. Mandrus, L. Zhao. Electric quadrupole second-harmonic generation revealing dual magnetic orders in a magnetic Weyl semimetal. *Nat. Photonics* **18**, 26 (2024).
- [29] S. A. Yang, X. Li, A. D. Bristow, J. E. Sipe. Second harmonic generation from tetragonal centrosymmetric crystals. *Phys. Rev. B* **80**, 165303 (2009).
- [30] N. D. Mermin, H. Wagner. Absence of Ferromagnetism or Antiferromagnetism in One- or Two-Dimensional Isotropic Heisenberg Models. *Phys. Rev. Lett.* **17**, 1133 (1966).
- [31] E. Yi, D. F. Zheng, F. Pan, H. Zhang, B. Wang, B. Chen, D. Wu, H. Liang, Z. X. Mei, H. Wu, S. A. Yang, P. Cheng, M. Wang, B. Shen. Topological Hall effect driven by short-range magnetic order in EuZn_2As_2 . *Phys. Rev. B* **107**, 035142 (2023).
- [32] R. W. Boyd. *Nonlinear Optics* (Academic Press, 2020).
- [33] J. P. Sethna. *Entropy, Order Parameters, and Complexity* (Oxford University Press, 2006).
- [34] T. Schuh, T. Balashov, T. Miyamachi, A. F. Takács, S. Suga, W. Wulfhekel. Lifetimes of magnetic excitations in Fe and Co atoms and clusters on Pt(111). *J. Appl. Phys.* **107**, 09E156 (2010).
- [35] W. Bi, T. Culverhouse, Z. Nix, W. Xie, H.-J. Tien, T.-R. Chang, U. Dutta, J. Zhao, B. Lavina, E. E. Alp, D. Zhang, J. Xu, Y. Xiao, Y. K. Vohra. Drastic enhancement of magnetic critical temperature and amorphization in topological magnet EuSn_2P_2 under pressure. *npj Quant. Mater.* **7**, 43 (2022).
- [36] P. S. Pershan. Nonlinear Optical Properties of Solids: Energy Considerations. *Phys. Rev.* **130**, 919 (1963).
- [37] S. Mukamel, V. Khidekel, V. Chernyak. Classical chaos and fluctuation-dissipation relations for nonlinear response. *Phys. Rev. E* **53**, R1(R) (1996).
- [38] M. Fiebig, V. V. Pavlov, R. V. Pisarev. Second-harmonic generation as a tool for studying electronic and magnetic structures of crystals: review. *J. Opt. Soc. Am. B* **22**, 96 (2005).
- [39] K. L. Seyler, A. Ron, D. Van Beveren, C. R. Rotundu, Y. S. Lee, D. Hsieh. Direct visualization and control of antiferromagnetic domains and spin reorientation in a parent cuprate. *Phys. Rev. B* **106**, L140403 (2022).